Journal of Materials Chemistry A

PAPER

View Article Online
View Journal | View Issue

Cite this: J. Mater. Chem. A, 2018, 6, 15762

A low-cost Mg^{2+}/Na^{+} hybrid aqueous battery†

Xi Cao, Lulu Wang, Jitao Chen* and Junrong Zheng*

Received 26th May 2018
Accepted 18th July 2018

DOI: 10.1039/c8ta04930k

rsc.li/materials-a

A Mg^{2+}/Na^{+} hybrid aqueous battery with high energy density and low cost is constructed using commercial Mn_3O_4 as a cathode and $NaTi_2(PO_4)_3$ as an anode for the first time. During electrochemical cycling, spinel Mn_3O_4 experiences a transition to layered MnO_2 hosting Mg^{2+}/Na^{+} with a high specific capacity and a long cycling life in Mg^{2+}/Na^{+} hybrid electrolytes. The battery delivers a discharge potential above 1.2 V and an energy density over 47 W h kg^{-1} (based on the total mass of electrode materials) at a power density of 48 W kg^{-1}; even at a high power density of 400 W kg^{-1}, it delivers an energy density of 23.6 W h kg^{-1}. What is more, the battery shows an excellent cycling performance with 94% capacity retention after 6000 cycles at 10C. The performances drop only very slightly for batteries prepared by an economic and scalable method. The excellent electrochemical properties, combined with the low cost of raw materials and the ease of scaling up which many aqueous batteries lack, make this approach a very promising cost-effective environment-friendly solution for large-scale energy storage.

Introduction

Renewable energy sources such as natural wind and solar power have been experiencing fast growth recently due to the increasing need for clean energy. In general, the operations of these energy sources are not continuous and this often leads to low utilization.[1,2] To take full advantage of them, one approach is to convert the discontinuity into continuity by developing suitable energy storage systems, *e.g.* rechargeable batteries with high power, long cycle life and high energy efficiency for electric energy storage in a large scale.[3–6]

In today's energy storage market, lithium-ion and lead–acid batteries are the two major players. On one hand, the safety issues of lithium-ion associated with flammable organic electrolytes and the growing concerns of price and availability of Li resources impede their large-scale deployment. On the other hand, lead–acid batteries are safe aqueous systems, but the negative impact of lead on the environment besides their low energy density and limited cycling lifetime has been raising concerns about their future applications. Aqueous rechargeable batteries operating with earth abundant nontoxic elements (such as Na, K, Mg, Zn, *etc.*) as charge carriers thus re-emerge as promising alternative options.[7–12] Among them, aqueous sodium-ion batteries (SIBs) attract particular interest due to the abundance and low cost of Na ions. However, the relatively large radius of the sodium ion makes it difficult to insert into and extract from the electrode lattices. Even more serious is that unlike in organic ester/ether-based electrolytes, most Na-storage materials are not suitable to function as electrodes for aqueous SIBs owing to the limited voltage window defined by the potentials of H_2 evolution and O_2 evolution, as well as the chemical instability and electrochemical irreversibility in aqueous solutions. So far, only a handful of high-performance electrode materials for aqueous SIBs are available. Tunnel-structured oxides such as $Na_{0.44}MnO_2$, $Na_{0.66}Mn_{0.66}Ti_{0.34}O_2$ and Prussian-blue analogues such as $Na_2Ni[Fe(CN)_6]$ and $Na_2Cu[Fe(CN)_6]$ have been demonstrated to be able to function as the cathode of aqueous SIBs.[13–18] However, these materials do have problems like low capacity or poor cyclability owing to the large volume expansion during the intercalation/deintercalation of large Na^{+}.[19–21] On the anode side, NASICON-structured $NaTi_2(PO_4)_3$ is the most popular material because of its high specific capacity, reasonably high working potential (above the potential of H_2 evolution), and desirable ion-diffusion channels.[22–26] One drawback is that it may suffer from rapid capacity fading caused by severe side reactions in aqueous solutions. Nevertheless, this problem can be solved by appropriate carbon coating or structural design.[23–26]

The opposite occurs for aqueous rechargeable magnesium batteries (ARMBs). Cathode materials with excellent performances are well documented, for example, a series of magnesium manganese oxide molecular sieves (Mg-OMS) have been prepared and studied as the potential cathode material.[27,28] Besides Mg-OMS, it was recently reported that spinel Mn_3O_4 can be transformed into crystal-water-containing layered Birnessite MnO_2 during an electrochemical process in aqueous $MgSO_4$ electrolyte solutions[29,30] with a high capacity of about 240 mA h g^{-1} and an excellent cycle life (62.5% retention after 10 000 cycles). On the anode side, Mg metal cannot be used directly and it seems difficult to find a suitable anode material except activated carbon which often results in high cost and low energy density.[31]

College of Chemistry and Molecular Engineering, Beijing National Laboratory for Molecular Sciences, Peking University, Beijing 100871, China. E-mail: junrong@pku.edu.cn; chenjitao@pku.edu.cn

† Electronic supplementary information (ESI) available. See DOI: 10.1039/c8ta04930k

To solve the cathode problem of Na^+ batteries and the anode problem of Mg^{2+} batteries, we propose to combine these two battery systems into one, namely constructing a Mg^{2+}/Na^+ hybrid aqueous rechargeable battery system, in which spinel Mn_3O_4 is the cathode and $NaTi_2(PO_4)_3$ is the anode. Our results show that in the mixed Mg^{2+}/Na^+ electrolyte, spinel Mn_3O_4 experiences a phase transition to layered Birnessite MnO_2 and hosts the hydrated charge carriers, and $NaTi_2(PO_4)_3$ prefers hosting Na^+ in the hybrid electrolyte. In other words, owing to the size and hydration differences, the co-existence of Mg^{2+}/Na^+ does not significantly interfere with each other, which allows the battery to deliver a high discharge voltage to be above 1.2 V and a high reversible capacity above 47 W h kg^{-1} at the power density of 48 W kg^{-1}. This hybrid aqueous battery exhibits excellent cycling and rate performance; even at a high power density of 400 W kg^{-1}, it delivers an energy density of 23.6 W h kg^{-1} and 94% capacity retention after 6000 cycles. More importantly, a model battery assembled with commercial spinel Mn_3O_4 and a solid-state synthesized $NaTi_2(PO_4)_3$ hybrid which is scalable for large scale energy storage, exhibits an excellent cycling stability (with capacity retention of almost 100% after 1000 cycles) and energy density (39 W h kg^{-1}), which are comparable to the lead–acid batteries but with a much longer life span. What is more, both cathode and anode materials in this hybrid battery can be obtained with a low price compared to the price of lead (about 3000 dollars). The cathode can be obtained in bulk at the price of 13 000 RMB (about 2000 dollars) per ton, and can be directly used as received. As for the anode, among all precursors, the most expensive material is TiO_2, and can be acquired in bulk from chemical suppliers in China at the price of about 25 000 RMB (about 3750 dollar) per ton, fortunately, it only accounts for about 40 wt% in the final products. Thus, even with other precursors, the cost of the anode is estimated to be no more than 20 000 RMB (about 3000 dollar) per ton. Thus, from the view of the cost of both anode and cathode sides, the cost of this hybrid battery is estimated to be comparable to the lead–acid batteries either. The excellent electrochemical performances, combined with the low cost of raw materials and the ease of scaling up which many aqueous batteries lack, make this approach a very promising low cost and environment-friendly solution for large scale energy storage.

Results

Two types of batteries are assembled and tested in this work. The first one is a proof of concept with commercial Mn_3O_4 as the cathode, sol–gel-synthesized $NaTi_2(PO_4)_3$ as the anode, and a mixed 2 M $MgSO_4$–1 M Na_2SO_4 aqueous solution as the electrolyte. The second one is a model battery that can be scaled up for low-cost large scale energy storage with solid-state-synthesized $NaTi_2(PO_4)_3$ as the anode.

Electrochemical performance of the Mn_3O_4//sol–gel-synthesized $NaTi_2(PO_4)_3$–G–C hybrid aqueous battery

The electrochemical performance of the proof-of-concept battery is evaluated. The weight ratio of the Mn_3O_4 cathode and the sol–gel synthesized $NaTi_2(PO_4)_3$–G–C anode in the full cell is ~1.5 : 1, which is an anode-limited cell design. Fig. 1a and b show potential–time curves *vs.* the Ag/AgCl reference electrode, and the first charge/discharge curves of the full cell at a current density of 1C (1C = 100 mA g^{-1} in this work, based on the mass of the anode) within the cut-off voltage window of 0.4–1.85 V, respectively. The average discharge voltage of the full cell is about 1.2 V, with the cathode charge/discharge potential between 0 and 0.85 V and the anode potential from −0.4 to −1.0 V. The initial discharge capacity is 98 mA h g^{-1}. Changing the current density from 1C to 50C, the discharge capacity remains very stable and decreases gradually to 42 mA h g^{-1} (Fig. 1c and d). The battery exhibits excellent cycling stability, as shown in Fig. 1e and f. Its capacity retains 94% after 6000 cycles at 10C, and 100% after 200 cycles at 1C. Taking into account the total mass of the cathode and anode-active materials, the specific energy of the cells is 47 W h kg^{-1} at a power density of 48 W kg^{-1}, and 23.6 W h kg^{-1} at a high power of 400 W kg^{-1}. The results indicate that a $Mn_3O_4/NaTi_2(PO_4)_3$ system using a mild aqueous electrolyte is very promising for a high-performance, long-life, environmentally-friendly, and cost effective energy storage solution. We compared the electrochemical performances of this Mg^{2+}/Na^+ hybrid aqueous battery with other aqueous batteries; both energy density and the cycling performance are very remarkable among these aqueous batteries reported before (listed in Table S1†).

Reactions and structural evolution of the spinel Mn_3O_4 cathode

The cathode is made of industrial large-scale-produced Mn_3O_4. Its X-ray diffraction patterns are shown in Fig. 2a; the results match the standard crystallographic tables (JCPDS card 01-1127) very well, confirming the spinel crystal type of Mn_3O_4. The Mn_3O_4 powder is composed of 50 nm particles, revealed by the scanning electron microscopy (SEM) image in Fig. 2b and transmission electron microscopy (TEM) image in Fig. 2c. High resolution TEM image in Fig. 2d reveals that the *d* spacing of lattice fringes is 0.48 nm, which corresponds to the (101) plane from the peak at $2\theta = 18.1°$ in the XRD pattern.

In a mixed 2 M $MgSO_4$–1 M Na_2SO_4 aqueous solution, the cathode Mn_3O_4 particles gradually transform into lamellar structures consisting of nano-sheets, as shown in Fig. 3a. The morphology change is further investigated with XRD, TEM, and energy-dispersive X-ray spectroscopy (EDS). After 100 galvanostatic charge and discharge cycles in the potential range of −0.4 to 1.0 V, the spinel-Mn_3O_4 XRD peak disappears,[29,30,32] and peaks corresponding to layered-Birnessite MnO_2 appear (Fig. 3b). The (001) peak at 12.3° indicates that the layer-to-layer distance between octahedral MnO_6 is 7.25 Å. Such a spacing reflects the presence of crystal water between the MnO_6 layers.[33,34] The *d* spacings of lattice fringes of layered-Birnessite, 0.725 and 0.36 nm can be clearly observed from the HRTEM image (Fig. 3c).

EDS measurements suggest an interesting mechanism for the structural evolution. As shown in Fig. 3d, after the discharging process, both Mg^{2+} and Na^+ are present in the cathode

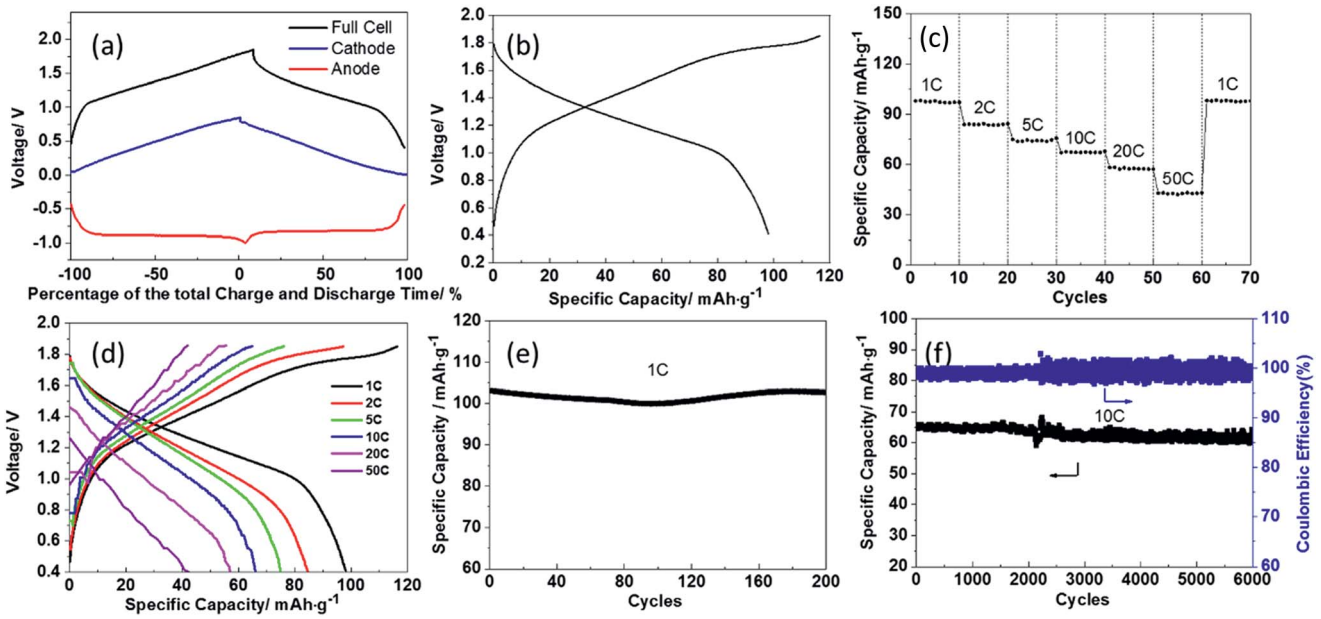

Fig. 1 (a) Percentage of total charge and discharge time of the full cell, cathode and anode materials. (b) Galvanostatic charge and discharge measurement of the full cell at 1C. (c and d) Rate performance. (e) Cycling performance at 1C. (f) Cycling performance at the current density of 10C (1C = 100 mA g^{-1}).

and Mg^{2+} is the dominant species. However, after the charging process, only Na^+ exists (Fig. 3e). The results suggest that during the charging process, Na^+ but not Mg^{2+} inserts into the interlayer space between MnO_6 layers, but in the discharging process both the cations can insert into the cathode and the insertion of Mg^{2+} is easier. The insertion during charging is probably chemically driven in the reverse (reducing) direction to the applied anodic (oxidizing) electric field, stabilizing the structure and recovering the charge balance following the deinsertion of Mn^{2+},[34] as illustrated in Fig. 3f. Besides Na^+, water in the form of the hydrated proton is also suggested to insert into the cathode.[34] It is interesting to note that it is Na^+ but not Mg^{2+} that can insert into the lattice. The results can be rationalized if hydrated rather than bare cations carry the insertion, which is

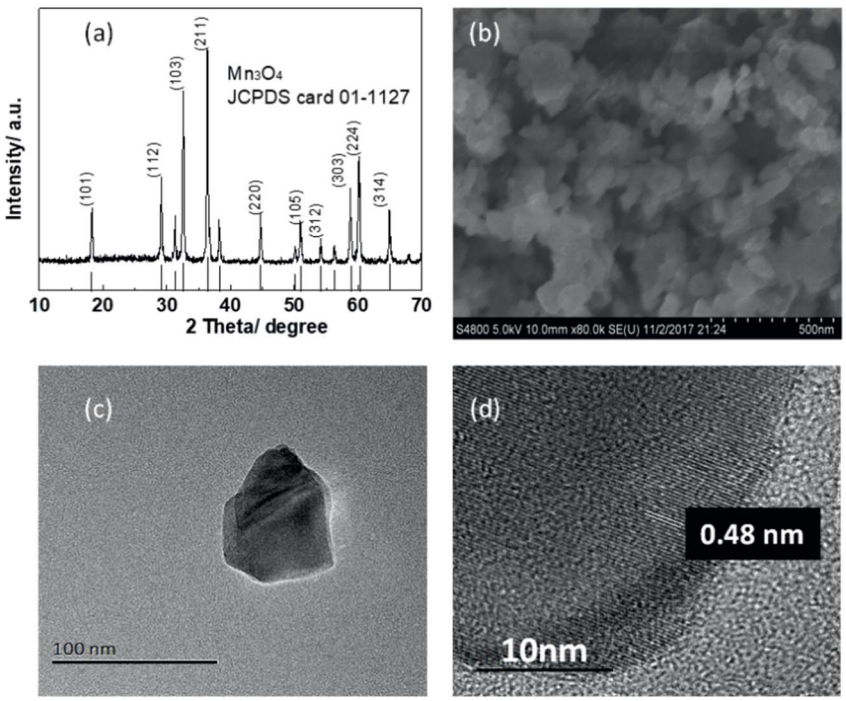

Fig. 2 (a) X-ray diffraction patterns of commercial Mn_3O_4. (b) SEM image of Mn_3O_4. (c) TEM image of Mn_3O_4. (d) HRTEM image of Mn_3O_4.

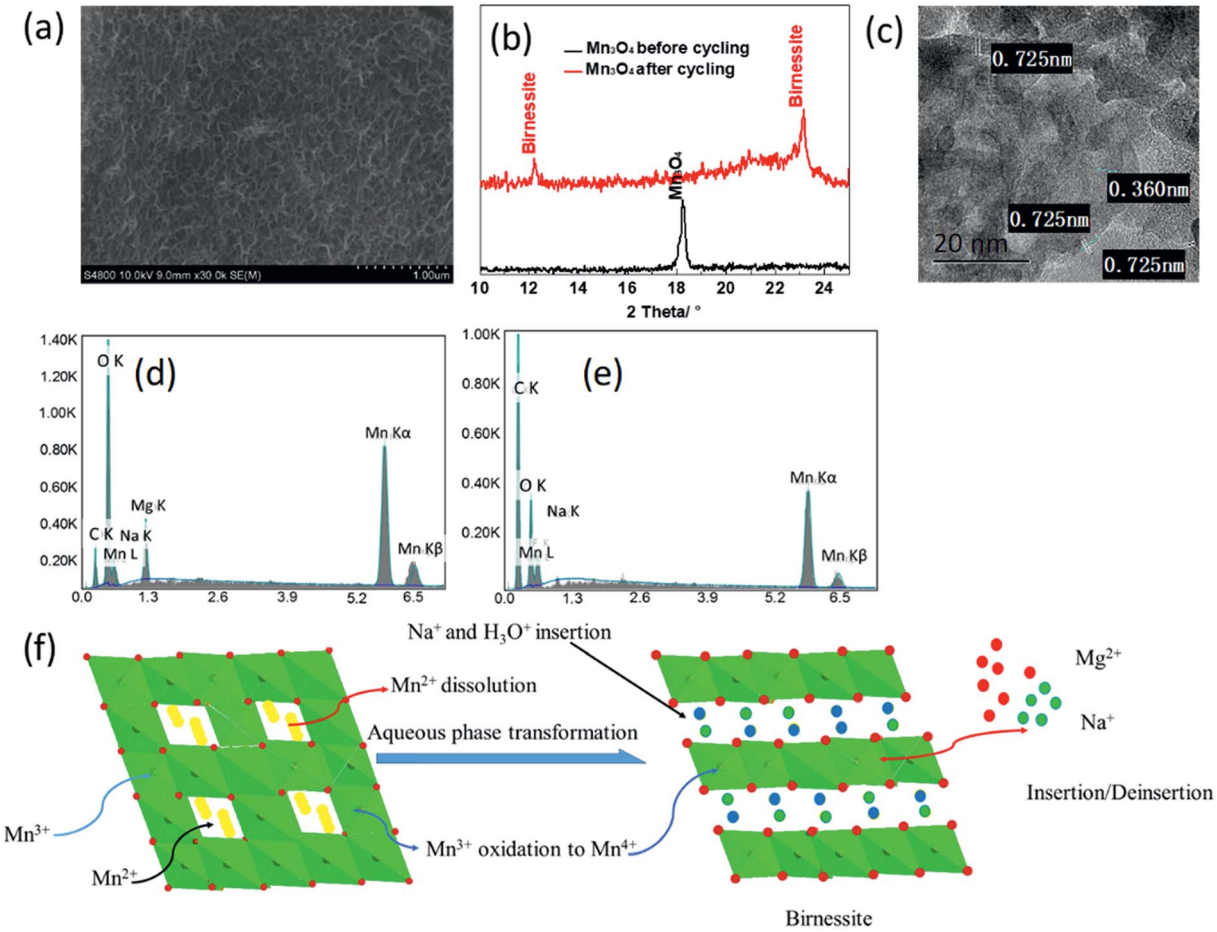

Fig. 3 Structural change of the cathode in the mixed 2 M $MgSO_4$–1 M Na_2SO_4 aqueous solution. (a) SEM image of the cathode after 100 charge/discharge cycles. (b) The X-ray diffraction patterns of Mn_3O_4 before (black) and after (red) cycling. (c) HRTEM image of the cathode after cycling. (d) EDS of the cathode after discharge. (e) EDS of the cathode after charge. (f) Illustration of initial transition of the cathode material.

very conceivable because of the relatively positive potential during charging. Besides the much larger charge density, the radius of hydrated Mg^{2+} of about 4.3 Å significantly larger than that of the hydrated Na^+ (3.6 Å) or that of the hydrated proton (~3.5 Å, $H_3O^+(H_2O)_6$)[35,36] may well block it from entering the lattice. The situation is opposite in the discharging process. The negative potential provides a sufficiently strong driving force for cations to dehydrate and insert into the lattice likely in the form of bare cations. The smaller radius of bare Mg^{2+} (0.72 Å) than Na^+ (1.02 Å) can probably facilitate its motion inside the lattice over larger cations. The proposed mechanism is further supported by experiments in electrolytes of individual cations, as elaborated in the following.

The galvanostatic charge and discharge measurement results of Mn_3O_4 in 2 M $MgSO_4$, 1 M Na_2SO_4, and 2 M $MgSO_4$–1 M Na_2SO_4 hybrid electrolytes are respectively shown in Fig. 4a–c. Distinct discharge profiles in different electrolytes are observed. The spinel Mn_3O_4 cathode exhibits a larger discharge capacity of 130 mA h g^{-1} in 2 M $MgSO_4$ than 97 mA h g^{-1} in 1 M Na_2SO_4. Both specific capacities increase over cycles, indicating that activation is required to complete the phase transition of all cathode Mn_3O_4 particles. The discharge voltage plateau is also higher in the Mg^{2+} solution than in the Na^+ solution. The performances in the mixed solution lie between (Fig. 4d) those in other two electrolytes. The results can be well explained by the mechanism described below. Both Na^+ and Mg^{2+} can insert into the lattice during discharging, producing capacities. The easier insertion of Mg^{2+} results in a larger capacity and a higher voltage. EDS measurements show a much larger extent of Mg^{2+} insertion than Na^+ (Fig. S1a and b in ESI†), consistent with the results in the mixed solution. Cyclic voltammetry (CV) scans also confirm the results. The wide reduction peak at around 0 V (Fig. 4e) corresponding to the insertion process of magnesium ions into the lattice in the Mg^{2+} solution shifts to around −0.3 V (Fig. 4f) in pure Na_2SO_4. The two oxidation peaks at around 0.5 V and 0.3 V corresponding to the deinsertion process of magnesium ions from the lattice in 2 M $MgSO_4$ electrolyte (Fig. 4e) become less pronounced and shift to lower voltage in the Na^+ solution, indicating an easier Mg^{2+} insertion/deinsertion kinetics. In the mixed solution, the reduction/oxidation peaks (Fig. 4g and h) of both cations coexist.

Besides the EDS and CV studies, we also conduct the XRD and XPS characterization to verify the insertion/extraction mechanism of Mg^{2+}/Na^+, the detailed discussion can be found in the ESI.†

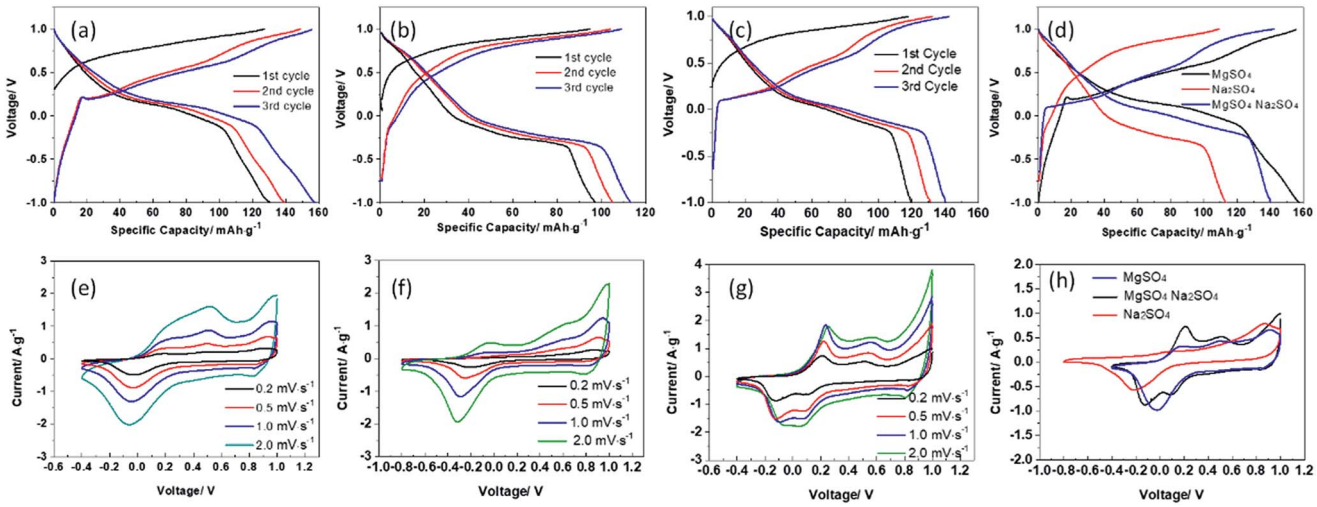

Fig. 4 Galvanostatic charge and discharge measurement of Mn_3O_4 in different electrolytes in the potential range from −1.0 to +1.0 V. (a) 2 M $MgSO_4$. (b) 1 M Na_2SO_4. (c) 2 M $MgSO_4$–1 M Na_2SO_4 hybrid electrolytes. (d) Comparison of the 3rd cycle. Cyclic voltammetry (CV) of Mn_3O_4 in different electrolytes at scan rates of 0.2, 0.5, 1.0, and 2.0 mV s^{-1}. (e) 2 M $MgSO_4$. (f) 1 M Na_2SO_4. (g) 2 M $MgSO_4$–1 M Na_2SO_4 hybrid electrolytes. (h) Comparison of the three CV curves at the scan rate of 0.2 mV s^{-1}.

The electrochemical behavior of Mn_3O_4 in the potential range from 0 to +0.85 V (the working potential of the cathode in full battery) in different electrolytes is also investigated, as shown in Fig. 5. Similar to the above results, the spinel Mn_3O_4 cathode exhibits larger discharge capacity in 2 M $MgSO_4$ than in 1 M Na_2SO_4, and lies between these two capacities in the hybrid electrolyte. Both the rate and cycling performance of the spinel Mn_3O_4 cathode in 2 M $MgSO_4$ and 2 M $MgSO_4$–1 M Na_2SO_4 hybrid electrolytes are better than those in 1 M Na_2SO_4. Especially, the cathode in the hybrid electrolyte presents a higher reversible capacity of approximately 78.5 mA h g^{-1} at a current density of 1C and nearly 49.8 mA h g^{-1} even at a current density of 20C compared with that in pure Na_2SO_4 electrolyte. Even after 1000 charge/discharge cycles at 10C, it still remains 45.4 mA h g^{-1} with almost 80% capacity retention.

Structure and electrochemical performance of $NaTi_2(PO_4)_3$–G–C

The anode is a $NaTi_2(PO_4)_3$/carbon nanocomposite, denoted as $NaTi_2(PO_4)_3$–G–C, made from a sol–gel method. It contains 30–50 nm NASICON $NaTi_2(PO_4)_3$ particles (Fig. 6, crystal structure indexed to JCPDS card no. 33-1296) coated with a dense coated-carbon layer with a thickness of ~7 nm dispersed on the reduced graphene oxide (rGO) nanosheets. The carbon content in $NaTi_2(PO_4)_3$–G–C is determined to be 16.7% by the TGA analysis (Fig. S3a†). This "poached egg" structure not only contains rGO as the support, but also contains a coated carbon layer on the surface of $NaTi_2(PO_4)_3$ particles, which constitutes a highly conductive bicontinuous pathway surrounding the particle surface and across the particles. On one hand, the uniform carbon coating layer can also create a protective barrier that prevents the aggregation and growth of $NaTi_2(PO_4)_3$ particles. On the other hand, the nanoparticles anchored on the surface of rGO can act as spacers to prevent the restacking of rGO and thus the loss of highly active surface area.[23,24,37]

Different from the cathode where both Mg^{2+} and Na^+ can enter the host lattice, the anode only allows Na^+ to access. As shown in Fig. 7a, in the $MgSO_4$ electrolyte, the CV curves of $NaTi_2(PO_4)_3$–G–C show no obvious reduction/oxidation peaks, indicating very few Mg^{2+} inserted into $NaTi_2(PO_4)_3$, which can

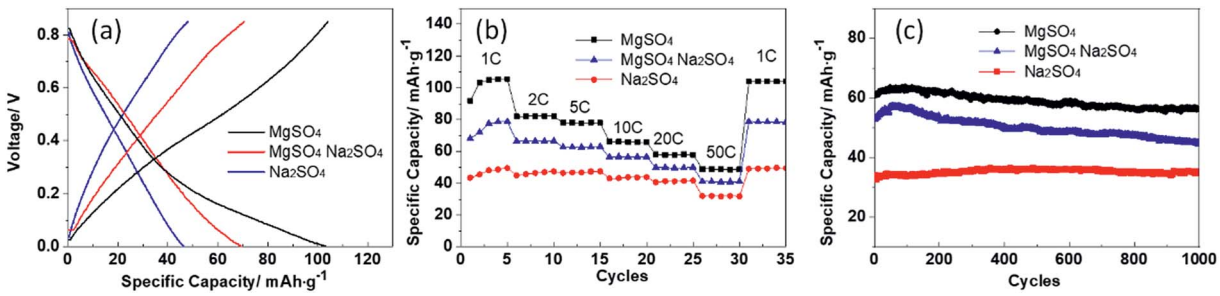

Fig. 5 (a) Galvanostatic charge and discharge measurement of Mn_3O_4 in different electrolytes in the potential range from 0 to +0.85 V at the current density of 1C. (b) Rate performance of Mn_3O_4 in different electrolytes. (c) Cycling performance of Mn_3O_4 in different electrolytes at the current density of 10C.

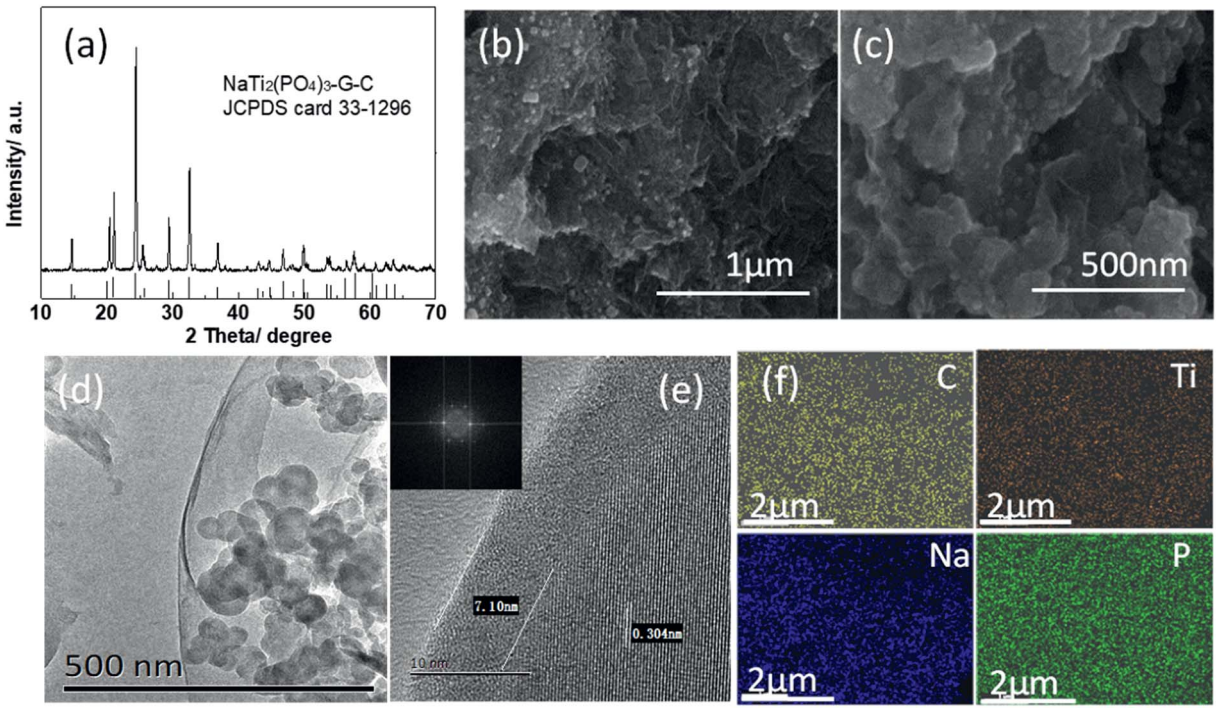

Fig. 6 (a) The crystal structure of $NaTi_2(PO_4)_3$–G–C. (b and c) SEM image of $NaTi_2(PO_4)_3$–G–C. (d) TEM image of $NaTi_2(PO_4)_3$–G–C. (e) HRTEM image of $NaTi_2(PO_4)_3$–G–C. (f) EDS mapping of $NaTi_2(PO_4)_3$–G–C.

also be evidenced by the EDS results of $NaTi_2(PO_4)_3$ after cycling in $MgSO_4$ electrolytes (Fig. S4†). In the Na^+ solution and mixed solution (Fig. 7b and c), a pair of redox peaks appear at about −0.88 V (reduction) and −0.83 V (oxidation) *versus* the Ag/AgCl reference electrode, corresponding to the Ti^{4+}/Ti^{3+} redox peaks during the extraction/insertion process of Na^+ in the NASICON-type structured $NaTi_2(PO_4)_3$.[25,38–40] The redox reaction can therefore take place at potentials much more positive than the H_2 evolution potential of water. In the mixed solution, the anode material has excellent electrochemical performance with a capacity of 70 mA h g^{-1} (10C) which still retains almost 100% after 1000 charge/discharge cycles. The superior performance of $NaTi_2(PO_4)_3$–G–C may be attributed to the stable crystal structure of $NaTi_2(PO_4)_3$, the excellent electronic conductivity of rGO

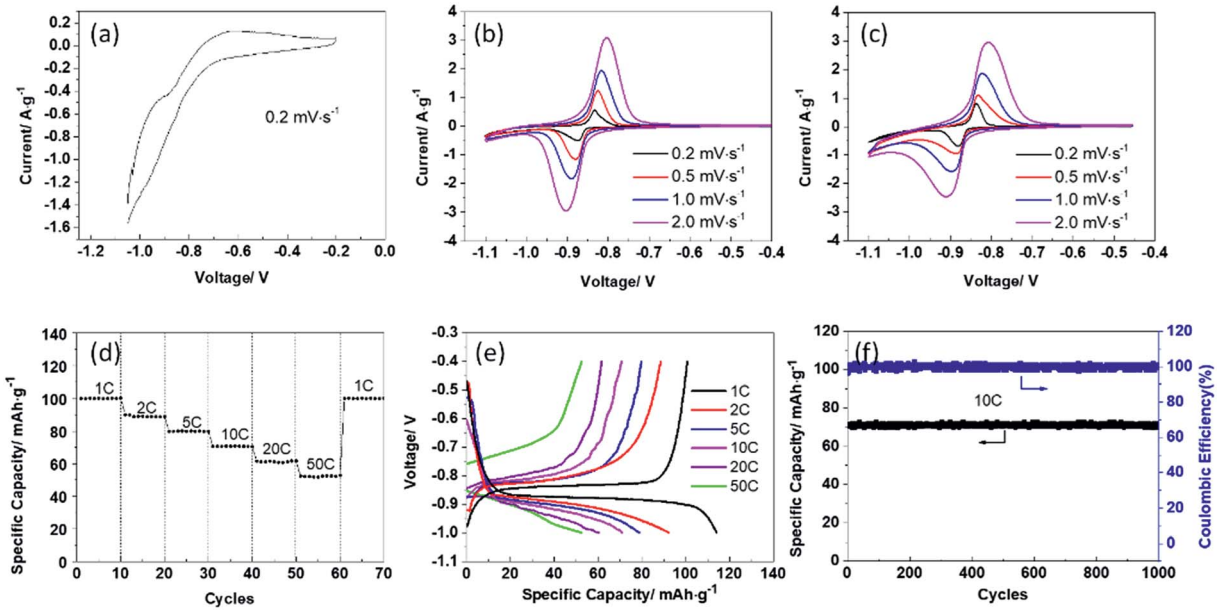

Fig. 7 CV of $NaTi_2(PO_4)_3$–G–C in different electrolytes. (a) 2 M $MgSO_4$. (b) 1 M Na_2SO_4. (c) 2 M $MgSO_4$–1 M Na_2SO_4 hybrid electrolytes. (d and e) Rate performance. (f) Cycling performance of $NaTi_2(PO_4)_3$–G–C in hybrid electrolytes at 10C.

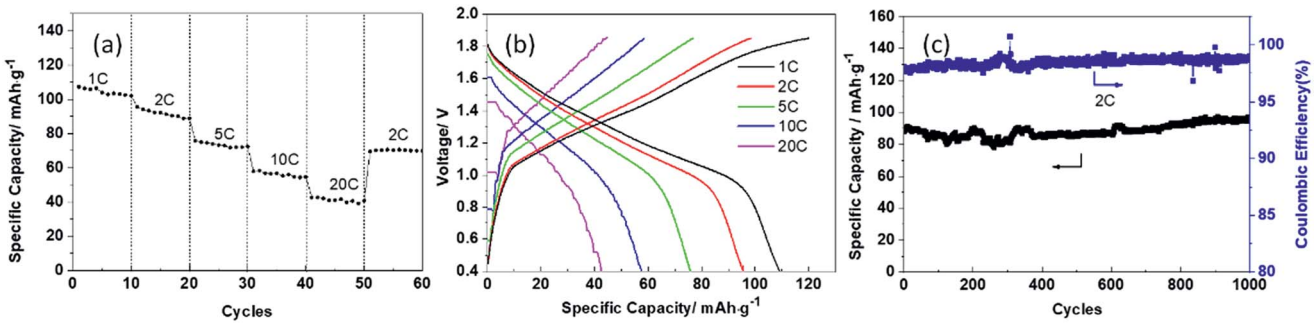

Fig. 8 (a and b) Rate performance of Mn_3O_4//$NaTi_2(PO_4)_3$–S hybrid aqueous battery. (c) Cycling performance at the current density of 2C.

and conductive carbon layer, which not only keep the integral stability of the electrode material in the long cycling process, but also ensure a high rate capability.[23,37,41,42]

The electrochemical performance of the full cell constructed from Mn_3O_4 and $NaTi_2(PO_4)_3$–G–C after cycling in a three electrode cell is also studied, as shown in Fig. S5.† The specific capacity and the cycling stability are similar to the full cell using Mn_3O_4 and $NaTi_2(PO_4)_3$–G–C directly, which indicates that the phase transition process in the full cell has little effect on the performance.

Electrochemical performance of the Mn_3O_4//$NaTi_2(PO_4)_3$–S hybrid aqueous battery

The proof-of-concept battery described above works very well. However, the sol–gel method to prepare the anode material is very difficult and extremely costly to scale up. We therefore prepare the anode material from a solid state synthesis method that can be easily scaled up but more difficult to control the particle size of $NaTi_2(PO_4)_3$. A battery assembled with this anode, denoted as $NaTi_2(PO_4)_3$–S, and commercial Mn_3O_4, and 2 M $MgSO_4$/1 M Na_2SO_4, which can be scaled up to massive production at low cost, also exhibits excellent properties. The detailed structure analysis of $NaTi_2(PO_4)_3$–S can be found in the ESI.† Its rate and cycle performances are shown in Fig. 8. It presents a high reversible capacity of approximately 106 mA h g^{-1} at a current density of 1C and nearly 40 mA h g^{-1} even at a current density of 20C, more significantly, the full cell also displays a good capacity recovery when the current density switches back from 20C to 2C, demonstrating the excellent high rate performance and good electrode stability. It retains 100% of the capacity after 1000 cycles at 2C with nearly 100% coulombic efficiency. The specific energy of the cells is 39 W h kg^{-1} at a power density of 96 W kg^{-1}. The energy density is comparable to those of lead–acid batteries but with a much longer life span. What is more, as mentioned before, both cathode and anode materials in this hybrid battery can be obtained at a low price compared to lead. Thus, the cost of this hybrid battery is estimated to be low compared to the lead–acid batteries either.

Conclusion

In summary, we successfully construct a Mg^{2+}/Na^+ hybrid aqueous battery using commercial Mn_3O_4 as the cathode and $NaTi_2(PO_4)_3$ as the anode for the first time. This hybrid aqueous battery is capable of exceptionally high charge/discharge rates (over 10C) and stable cycling up to 6000 cycles, delivering an energy density about 23 W h kg^{-1}. These remarkable electrochemical properties, combined with the low cost of raw materials and scalable preparation and assembly methods, enable the Mg^{2+}/Na^+ hybrid aqueous battery to become a promising candidate for a safe, low cost, and environment-friendly large scale energy storage system.

Materials preparation and characterization

Preparation of the cathode material

Mn_3O_4 is bought from GeRui Corporation (Hunan, China) and used directly as received. Mn_3O_4 and conductive carbon with the mass ratio of 8 : 1 are mixed in a planetary ball mill (with the diameter of milling media about 5 mm) for 120 min at a speed of 500 rpm.

Preparation of $NaTi_2(PO_4)_3$–carbon materials through a sol–gel method

First, 0.01 M citric acid (Sigma-Aldrich, 99.99%) solution is prepared. The stoichiometric amounts of sodium carbonate (1 mmol, Sigma-Aldrich, 99.9%), titanium butoxide (4 mmol, Sigma-Aldrich, 99.9%), and monoammonium phosphate (6 mmol, Sigma-Aldrich, 99.9%) with the molar ratio of sodium : citric acid equals to 1 : 1 is mixed. 100 mg of graphene oxide (GO, obtained from XianFeng Nano Tech.) and 0.2 g cetyltrimethylammonium bromide (CTAB) are put into the above solution with continuous vigorous stirring for several hours. Then, the solution is dried at 80 °C. After preheating at 350 °C for 1 h and sintering at 800 °C for 1 h under an Ar atmosphere, this $NaTi_2(PO_4)_3$–carbon (denoted as $NaTi_2(PO_4)_3$–G–C) is obtained.

Preparation of $NaTi_2(PO_4)_3$–carbon materials through a scalable solid state method

A scalable solid state method is also used to prepare the $NaTi_2(PO_4)_3$–carbon (denoted as $NaTi_2(PO_4)_3$–S) composite. The precursor mixture containing 1 : 2 : 2 molar ratio of monobasic NaH_2PO_4 (99% pure Sigma Aldrich), TiO_2 (Aladdin P25), and

dibasic $(NH_4)_2HPO_4$ (>98%, Sigma Aldrich) with 5% carbon black and 5% natural graphite are planetary ball milled for approximately 120 min with the diameter of milling media about 5 mm at the speed of 500 rpm. The resulting precursor mixture is placed in a vacuum oven at 350 °C for 1 h and sintered at 800 °C for 1 h under an Ar atmosphere to obtain $NaTi_2(PO_4)_3$–S.

Materials characterization method

The crystal structures of both anode and cathode sides are identified using a X-ray diffractometer (XRD, Rigaku) with Cu Kα radiation. Transmission electron microscopy (TEM) measurements are conducted on a H9000NAR microscope (Hitachi, Japan) equipped with a cold field-emission gun operating at 200 kV accelerating voltage. The samples are suspended in ethanol and transferred onto a Cu grid for TEM measurements. The scanning electron microscopy (SEM) is performed to investigate the morphology of the electrode materials before and after electrochemical cycling. The content of carbon in the anode materials is determined from the mass loss of the samples at 800 °C in an air atmosphere with a Q50 thermogravimetric (TGA) apparatus (TA, USA). X-ray photoelectron spectroscopy (XPS) analysis of the active materials is performed using a Surface Science Instruments S-probe spectrometer.

Electrochemical measurement of the electrode materials

The prepared cathode/anode slurry is made up of 10% conductive carbon black, 10% polyvinylidene difluoride (PVDF) binder and 80% active material dispersed in 1-methyl-2-pyrrolidone (NMP). The obtained electrodes are prepared by coating the slurry onto graphite paper (with the thickness of 100 μm) with mass loadings of active material about 5 mg cm^{-2}, and then the electrodes are dried in a vacuum at 80 °C for 24 h. A LAND Battery Testing system (model CT2001A, Land, China) is used to measure the galvanostatic charge and discharge tests. The electrochemical workstation (CHI 650C, US) is used to test cyclic voltammetry (CV). The electrochemical tests of the electrode are performed by utilizing a conventional standard three electrode electrochemical cell, including a working electrode, a counter electrode (Pt sheet) and a reference electrode (Ag/AgCl) in 2 M $MgSO_4$, 1 M Na_2SO_4 and 2 M $MgSO_4$–1 M Na_2SO_4 hybrid electrolytes.

Electrochemical measurement of the full cell

Full cells are fabricated using spinel Mn_3O_4 as the cathode and $NaTi_2(PO_4)_3$–C composite as the anode, with the filter paper as the traditional battery separator. 2 M $MgSO_4$–1 M Na_2SO_4 is used as the electrolyte in a sandwich-type coin. Galvanostatic discharge and charge measurements are performed at different current densities in the voltage range of 0.4–1.85 V. Cyclic voltammetry (CV) and impedance studies are conducted on CHI650C, in which impedance is recorded with an amplitude of 5.0 mV in the frequency range from 100 kHz to 0.01 Hz.

Conflicts of interest

There are no conflicts to declare.

Acknowledgements

This work was supported by the National Natural Science Foundation of China NSFC (NSFC-21673004, 21673008) and MOST (2017YFA0204702) China and China Postdoctoral Science Foundation (grant 2017M610017).

References

1 M. Armand and J. M. Tarascon, *Nature*, 2008, **451**, 652–657.
2 B. Dunn, H. Kamath and J. M. Tarascon, *Science*, 2011, **334**, 928–935.
3 Z. Chang, Y. Yang, M. Li, X. Wang and Y. Wu, *J. Mater. Chem. A*, 2014, **2**, 10739–10755.
4 P. Simon and Y. Gogotsi, *Nat. Mater.*, 2008, **7**, 845–854.
5 M. R. Lukatskaya, B. Dunn and Y. Gogotsi, *Nat. Commun.*, 2016, **7**, 12647.
6 S. Chu and A. Majumdar, *Nature*, 2012, **488**, 294–303.
7 S. Liu, J. J. Hu, N. F. Yan, G. L. Pan, G. R. Li and X. P. Gao, *Energy Environ. Sci.*, 2012, **5**, 9743–9746.
8 B. Zhang, Y. Liu, X. Wu, Y. Yang, Z. Chang, Z. Wen and Y. Wu, *Chem. Commun.*, 2014, **50**, 1209–1211.
9 F. Wang, F. Yu, X. Wang, Z. Chang, L. Fu, Y. Zhu, Z. Wen, Y. Wu and W. Huang, *ACS Appl. Mater. Interfaces*, 2016, **8**, 9022–9029.
10 X. Wu, Y. Li, Y. Xiang, Z. Liu, Z. He, X. Wu, Y. Li, L. Xiong, C. Li and J. Chen, *J. Power Sources*, 2016, **336**, 35–39.
11 M. H. Alfaruqi, V. Mathew, J. Gim, S. Kim, J. Song, J. P. Baboo, S. H. Choi and J. Kim, *Chem. Mater.*, 2015, **27**, 3609–3620.
12 Y. Liu, Y. Qiao, W. X. Zhang, H. H. Xu, Z. Li, Y. Shen, L. X. Yuan, X. L. Hu, X. Dai and Y. H. Huang, *Nano Energy*, 2014, **5**, 97–104.
13 C. Deng, S. Zhang, Z. Dong and Y. Shang, *Nano Energy*, 2014, **4**, 49–55.
14 Z. G. Hou, X. N. Li, J. W. Liang, Y. C. Zhu and Y. T. Qian, *J. Mater. Chem. A*, 2015, **3**, 1400–1404.
15 D. J. Kim, Y. H. Jung, K. K. Bharathi, S. H. Je, D. K. Kim, A. Coskun and J. W. Choi, *Adv. Energy Mater.*, 2014, **4**, 1400133.
16 H. Gao and J. B. Goodenough, *Angew. Chem.*, 2016, **128**, 12960–12964.
17 T.-F. Hung, H.-L. Chou, Y.-W. Yeh, W.-S. Chang and C.-C. Yang, *Chem.–Eur J.*, 2015, **21**, 15686–15691.
18 G. Pang, P. Nie, C. Z. Yuan, L. F. Shen, X. G. Zhang, J. J. Zhu and B. Ding, *Energy Technol.*, 2014, **2**, 705–712.
19 X. Q. Zhang, Z. G. Hou, X. N. Li, J. W. Liang, Y. C. Zhu and Y. T. Qian, *J. Mater. Chem. A*, 2016, **4**, 856–860.
20 F. Zhang, W. Li, X. Xiang and M. Sun, *Chem.–Eur J.*, 2017, **23**, 12944–12948.
21 Y. S. Wang, L. Q. Mu, J. Liu, Z. Z. Yang, X. Q. Yu, L. Gu, Y. S. Hu, H. Li, X. Q. Yang, L. Q. Chen and X. J. Huang, *Adv. Energy Mater.*, 2015, **5**, 1501005.

22 A. I. Mohamed and J. F. Whitacre, *Electrochim. Acta*, 2017, **235**, 730–739.
23 X. Li, X. Zhu, J. Liang, Z. Hou, Y. Wang, N. Lin, Y. Zhu and Y. Qian, *J. Electrochem. Soc.*, 2014, **161**, A1181–A1187.
24 J. Song, S. Park, J. Gim, V. Mathew, S. Kim, J. Jo, S. Kim and J. Kim, *J. Mater. Chem. A*, 2016, **4**, 7815–7822.
25 M. Vujkovic, M. Mitric and S. Mentus, *J. Power Sources*, 2015, **288**, 176–186.
26 H. K. Roh, H. K. Kim, M. S. Kim, D. H. Kim, K. Y. Chung, K. C. Roh and K. B. Kim, *Nano Res.*, 2016, **9**, 1844–1855.
27 H. Zhang, K. Ye, K. Zhu, R. Cang, X. Wang, G. Wang and D. Cao, *ACS Sustainable Chem. Eng.*, 2017, **5**, 6727–6735.
28 H. Zhang, K. Ye, S. Shao, X. Wang, K. Cheng, X. Xiao, G. Wang and D. Cao, *Electrochim. Acta*, 2017, **229**, 371–379.
29 S. Kim, K. W. Nam, S. Lee, W. Cho, J.-S. Kim, B. G. Kim, Y. Oshima, J.-S. Kim, S.-G. Doo, H. Chang, D. Aurbach and J. W. Choi, *Angew. Chem., Int. Ed.*, 2015, **54**, 15094–15099.
30 K. W. Nam, S. Kim, S. Lee, M. Salama, I. Shterenberg, Y. Gofer, J.-S. Kim, E. Yang, C. S. Park, J. S. Kim, S.-S. Lee, W.-S. Chang, S. G. Doo, Y. N. Jo, Y. Jung, D. Aurbach and J. W. Choi, *Nano Lett.*, 2015, **15**, 4071–4079.
31 L. Wang, K. Asheim, P. E. Vullum, A. M. Svensson and F. Vullum-Bruer, *Chem. Mater.*, 2016, **28**, 6459–6470.
32 T. Xiong, W. S. V. Lee, X. Huang and J. M. Xue, *J. Mater. Chem. A*, 2017, **5**, 12762–12768.
33 X. Sun, V. Duffort, B. L. Mehdi, N. D. Browning and L. F. Nazar, *Chem. Mater.*, 2016, **28**, 534–542.
34 S. Kim, S. Lee, K. W. Nam, J. Shin, S. Y. Lim, W. Cho, K. Suzuki, Y. Oshima, M. Hirayama, R. Kanno and J. W. Choi, *Chem. Mater.*, 2016, **28**, 5488–5494.
35 J. Barthel and R. Jaenicke, *Berichte der Bunsengesellschaft für physikalische Chemie*, 1982, vol. 86, p. 264.
36 A. A. Zavitsas, *J. Phys. Chem. B*, 2001, **105**, 7805–7817.
37 B. D. Zhao, B. Lin, S. Zhang and C. Deng, *Nanoscale*, 2015, **7**, 18552–18560.
38 L. Chen, J. Y. Liu, Z. W. Guo, Y. G. Wang, C. X. Wang and Y. Y. Xia, *J. Electrochem. Soc.*, 2016, **163**, A904–A910.
39 S. I. Park, I. Gocheva, S. Okada and J. Yamaki, *J. Electrochem. Soc.*, 2011, **158**, A1067–A1070.
40 Z. Huang, L. Liu, L. Yi, W. Xiao, M. Li, Q. Zhou, G. Guo, X. Chen, H. Shu, X. Yang and X. Wang, *J. Power Sources*, 2016, **325**, 474–481.
41 Y. Jiang, J. A. Shi, M. Wang, L. C. Zeng, L. Gu and Y. Yu, *ACS Appl. Mater. Interfaces*, 2016, **8**, 689–695.
42 B. D. Zhao, Q. Y. Wang, S. Zhang and C. Deng, *J. Mater. Chem. A*, 2015, **3**, 12089–12096.